Journal of Radioanalytical and Nuclear Chemistry (2019) 319:737–748
https://doi.org/10.1007/s10967-018-6379-y

One-step synthesis of magnetic composite UiO-66/Fe_3O_4/GO for the removal of radioactive cesium ions

Sheng Feng[1] · Ziqiu Ni[1] · Shanshan Feng[1] · Zhihui Zhang[2] · Shuguang Liu[1] · Runbai Wang[1] · Jiawei Hu[1]

Received: 10 August 2018 / Published online: 8 January 2019

Abstract
In this study, the UiO-66/Fe_3O_4/GO composite was prepared by one step method for removal of cesium ions (Cs^+) in water and exhibited excellent adsorption capacity for Cs^+ (62.07 mg g^{-1}), which can be attributed to the size compatibility of nano-sized cavities and the addition of GO. As supporting matrix, GO decreased particle aggregation and increased the surface area of the adsorbent. The composite had good acid and alkali resistance, thermal stability, rapid adsorption rate and can be separated from water by magnetic separation rapidly.

Keywords UiO-66/Fe_3O_4/GO · Adsorption · Cesium ions

Introduction

With the increase of global energy demand and the strengthening of awareness of environmental protection, as a pivotal alternative energy source for fossil fuels, carbon-free nuclear power plays an important role in the development of human society [1]. However, the disposal of radioactive waste in nuclear fission still restricts the development of carbon-free nuclear power. Among them, radioactive cesium (^{137}Cs) is a radioactive substance produced during fission, accounting for 6.3% of fission products. It is the main cause of radioactive contamination and the most abundant species in nuclear power plant accidents and nuclear waste disposal [2, 3]. Radioactive cesium is strong gamma radiation source with long half-life ($T_{1/2}$ = 30.17 years) and similar to the biogeochemical behavior of potassium. It possesses outstanding mobility and causes serious threat to environment and human health via continuous flow in the food chain [4, 5]. Therefore, it is essential to eliminate radioactive ions to reduce radioactivity below the allowable range before long-term storage of nuclear waste. Among various processing techniques have been used to remove radionuclides cesium from aqueous solutions, adsorption is efficient, simple, flexible and affordable [6, 7]. The adsorption process does not use any toxic organic solvents [8]. But, many of these adsorbents are not provided with reproducibility and are often accompanied by environmental hazards. Thence, the effective and low-cost materials should be sought to selectively remove cesium-containing wastewater.

As porous materials composed of organic ligands linked with metal ions or ion clusters by coordination bonds [9], metal–organic frameworks (MOFs) have applications in various fields including gas storage, optics, sensing, catalysis, adsorption/separation, carbon dioxide capture and drug delivery [10–17]. Among various MOFs, UiO-66 is a three-dimensional porous zirconium-based MOF assembled from a 1,4-benzenedicarboxylic linkers and a cationic $Zr_6O_4(OH)_4$ nodes, having octahedral and tetrahedral cavities [18], which

✉ Sheng Feng
shfeng@cczu.edu.cn

✉ Shanshan Feng
fss728@163.com

Ziqiu Ni
ziqiuni@163.com

Zhihui Zhang
zhangzh@cczu.edu.cn

Shuguang Liu
shguangliu@163.com

Runbai Wang
892182568@qq.com

Jiawei Hu
15851987521@163.com

[1] School of Environmental and Safety Engineering, Changzhou University, Changzhou 213164, Jiangsu, China

[2] Jiangsu Key Laboratory of Advanced Catalytic Materials and Technology, Changzhou University, Changzhou 213164, Jiangsu, China

is known for their superior thermal, aqueous and acid stability [19]. Because of the merits of outstanding chemical stability and easy-to-synthesize, the potential application of UiO-66 has received significant concern. However, UiO-66 is usually present in form of powder and not conducive to be separated from solution. Magnetic separation can separate solid materials from liquid quickly and easily. Fe_3O_4 magnetic nanoparticles have been widely studied because of their low production cost, easy preparation and large-scale production capabilities [20]. However, magnetic nanomaterials have magnetic and large active surfaces, and the strong interparticle interactions between magnetic nanoparticles make them difficult to apply further [21]. Immobilization of magnetic nanoparticles on the substrate is a feasible method to stabilize Fe_3O_4 nanoparticles and reduce aggregation [22]. Graphene oxide (GO) is an ideal platform for the formation of new composites because of its hydrophilicity and availability of hydroxyl groups, epoxy and carbocyclic acid groups, which makes superior dispersibility in solution [23]. Moreover GO can also be used as an adsorbent. Fe_3O_4 magnetic nanoparticles are anchored on GO. The magnetization of the sorbent matrix promotes the recovery of the adsorbent used and provides a simple and viable solution for removing the target materials from the solution.

In this study, one step synthesis method was used to obtain UiO-66/Fe_3O_4/GO composite by loading nanoparticles composed of UiO-66 and Fe_3O_4 on GO. The composite was used to adsorb Cs^+ in water and compared with UiO-66 and UiO-66/Fe_3O_4 in terms of adsorption capacity. The initial Cs^+ concentration, contact time, temperature, pH and competing ions were studied about the effect on adsorption of Cs^+. Besides, the isotherm, kinetic, and thermodynamic models of the materials were also studied in detail.

Experimental

Materials

All reagents mentioned herein were from Aladdin Industrial Company, China and Sigma-Aldrich and used directly, including iron chloride hexahydrate ($FeCl_3{\cdot}6H_2O$), graphite powder, anhydrous ethanol, potassium permanganate, sulfuric acid, hydrogen peroxide (30%), zirconium tetrachloride ($ZrCl_4$, 98%), *p*-Phthalic acid (PTA, 99%), *N*,*N*-dimethylformamide (DMF, 99%), sodium hydroxide (NaOH, 97%), hydrochloric acid (HCl, 36.5%). All water used in the synthesis and treatment processes was deionized water.

Synthesis of UiO-66/Fe_3O_4 composite

Fe_3O_4 (0.1 g) was immersed to DMF (40 mL) and ultrasonicated for 30 min. The ultrasonic preparation frequencies mentioned herein are all 40 kHz and the power is 80 W. In addition, $ZrCl_4$ (0.15 g) and PTA (0.1062 g) were sequentially added to DMF (30 mL) and ultrasonicated for 10 min to obtain a MOF precursor solution. The Fe_3O_4 suspension was poured into the MOF precursor solution and ultrasonicated until the solid particles were evenly dispersed in the solution. The homogeneously mixed solution was poured into an autoclave (100 mL), placed in an oven at 80 °C for 12 h and then at 100 °C for 24 h. The resulting light brown solid was washed several times with ethanol and deionized water and separated from solution via magnetic separation. The purified UiO-66/Fe_3O_4 composite solids were obtained by freeze drying.

Synthesis of UiO-66/Fe_3O_4/GO composites (Fig. 1)

GO (0.03 g) was dissolved in DMF (80 mL) by ultrasonication for 5–8 h. Fe_3O_4 (0.075 g) was added to the mixture and ultrasonicated for 10 min. Then, $ZrCl_4$ (0.1125 g) was mixed in the above suspension and ultrasonicated for 30 min, followed by mechanical stirring for 12 h. Finally, 0.0797 g of PTA was added. After stirring in the mixture for 30 min, the treated suspension was charged in an autoclave (100 mL) and placed in an oven at 120 °C for 24 h. The synthesized solid was washed several times with ethanol and deionized water and separated from solution by magnetic separation. Finally, the nanocrystals were lyophilized.

Characterization

The scanning electron microscope (SEM) image was obtained by ZEISS Supra 55 microscope to analyze the appearance of the materials. Transmission electron microscope (TEM) (JEOL JEM-2100) can observe the microstructure of the samples. The powder X-ray diffraction (XRD) pattern was obtained using a Rigaku Dmax/Ultima IV diffractometer (Rigaku Co., Japan) to analyze the crystal structure and composition of materials. Fourier transform infrared spectroscopy (FTIR) was conducted at room temperature using a Spectrum One FTIR spectrophotometer (Perkin-Elmer, America). The materials were degassed at 395 K for 5 h before measuring the N_2 adsorption isotherm of the materials using the Micromeritics ASAP 2020 instrument (Micromeritics, American). The Brunauer–Emmet–Teller (BET) method estimated the surface area. Magnetization measurements used a vibrating sample magnetometer (VSM, Lakeshore 7404).

Adsorption experiments

In this study, inactive cesium (^{133}Cs) was used for the adsorption studies, instead of radioactive cesium (^{137}Cs). The Cs^+ solution (50.0 mL) was adsorbed by adsorbents (0.01 g) in a 50 mL sealed conical flask at a rotation speed

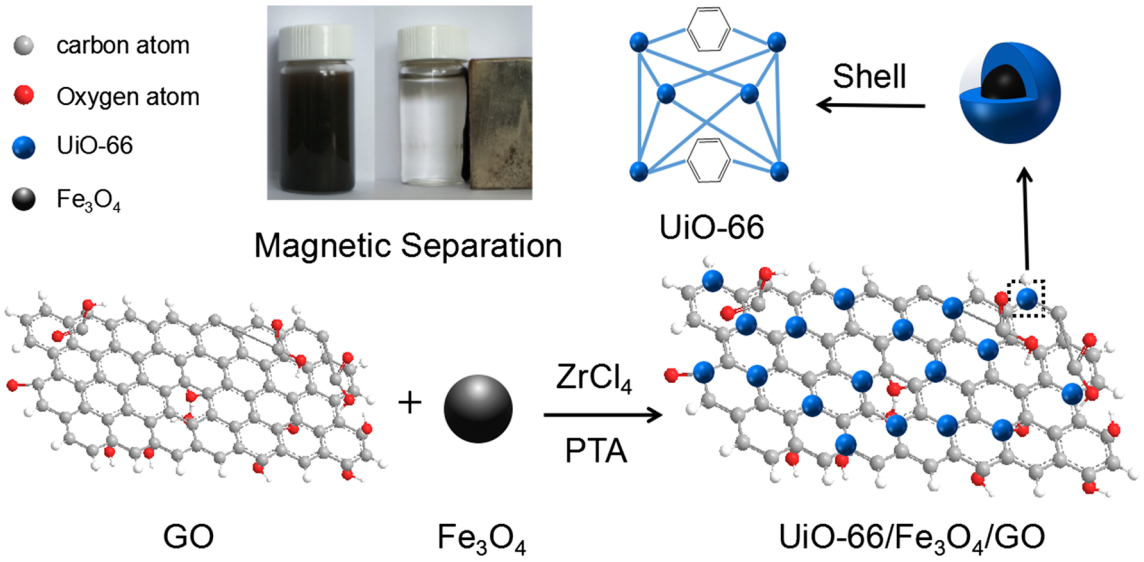

Fig. 1 Synthesis of UiO-66/Fe_3O_4/GO

of 200 rpm, and the temperature and rotation speed were controlled by a water bath shaker. The Cs^+ concentration was measured by an atomic absorption spectrophotometer (nov AA 300). In order to reduce the error of the experiment, three parallel tests were performed simultaneously in each experiment. The mass of Cs^+ adsorbed per unit mass of the adsorbent can be calculated by Eq. (1):

$$q_e = (C_0 - C_e) \times \frac{V}{m} \quad (1)$$

where C_0 (mg L^{-1}) is the initial Cs^+ concentration, C_e (mg L^{-1}) is the equilibrium Cs^+ concentration, m (g) is the mass of the adsorbents, V (L) is the volume of the Cs^+ solution.

Results and discussion

Characterization

The appearance and internal structure of the material were observed by SEM and TEM images. UiO-66/Fe_3O_4 nanoparticles (Fig. 2a) were agglomerated together in a spherical shape. Comparing Fig. 2a with Fig. 2b, it can be seen that the presence of GO did not change the spherical structure of the UiO-66/Fe_3O_4 nanoparticles, but the agglomeration phenomenon of the particles was reduced, and the small balls were disorderly dispersed in the wrinkles of the GO sheet. TEM images confirmed this statement.

The XRD patterns of Fe_3O_4, UiO-66, UiO-66/Fe_3O_4, UiO-66/Fe_3O_4/GO and GO were shown in Fig. 3. There were 7 diffraction peaks at 20°, 30°, 35°, 43°, 53°, 57° and 63° corresponding to (202), (220), (311), (400), (422), (511) and (440) diffracted planes of the pure cubic spinel crystal structure of Fe_3O_4 [24–26]. It can be observed that the diffraction peaks of Fe_3O_4 and UiO-66 were simultaneously present in the diffraction peaks of UiO-66/Fe_3O_4 diffraction pattern, indicating the successful synthesis of UiO-66/Fe_3O_4 composite. The diffraction pattern of UiO-66/Fe_3O_4 was similar to that of UiO-66/Fe_3O_4/GO, but the peak intensity of UiO-66/Fe_3O_4/GO can be found to be lower than that of UiO-66/Fe_3O_4 at 5°–10°. This can be attributed to the presence of very low levels of GO, and the diffraction peak of GO may be covered by the strong diffraction peak of UiO-66.

FTIR spectra of UiO-66/Fe_3O_4 in Fig. 4, characteristic of UiO-66 at 3423 cm^{-1}, 1577 cm^{-1}, and 1400 cm^{-1}, and Fe_3O_4 at 1654 cm^{-1} and 571 cm^{-1}, these peaks proved the formation of UiO-66/Fe_3O_4 composite. Comparing the peaks of UiO-66/Fe_3O_4, UiO-66/Fe_3O_4/GO was sharp at 1577–1654 cm^{-1}, which was due to the vibration of C=C skeleton in GO. And the presence of C–O stretching peak at 1095 cm^{-1} [27] further demonstrated the successful synthesis of UiO-66/Fe_3O_4/GO composite.

As shown in Fig. 5, the porosities and surface areas of all samples were measured by nitrogen adsorption–desorption at 77 K. The surface area of UiO-66 sample was 681.38 m^2 g^{-1}, which was similar to some of the reported results [28]. The curve of UiO-66 was a reversible type-I N_2 adsorption isotherm, which proved that UiO-66 exhibited permanent microporosity. The isotherms of the other two composites exhibited type-IV shape with H1 hysteresis loop by using the nitrogen adsorption–desorption measurements and BET method analysis. The type-IV isotherms illustrated that both materials had smaller mesoporous structures, and the appearance of the H1 hysteresis loop indicated that the

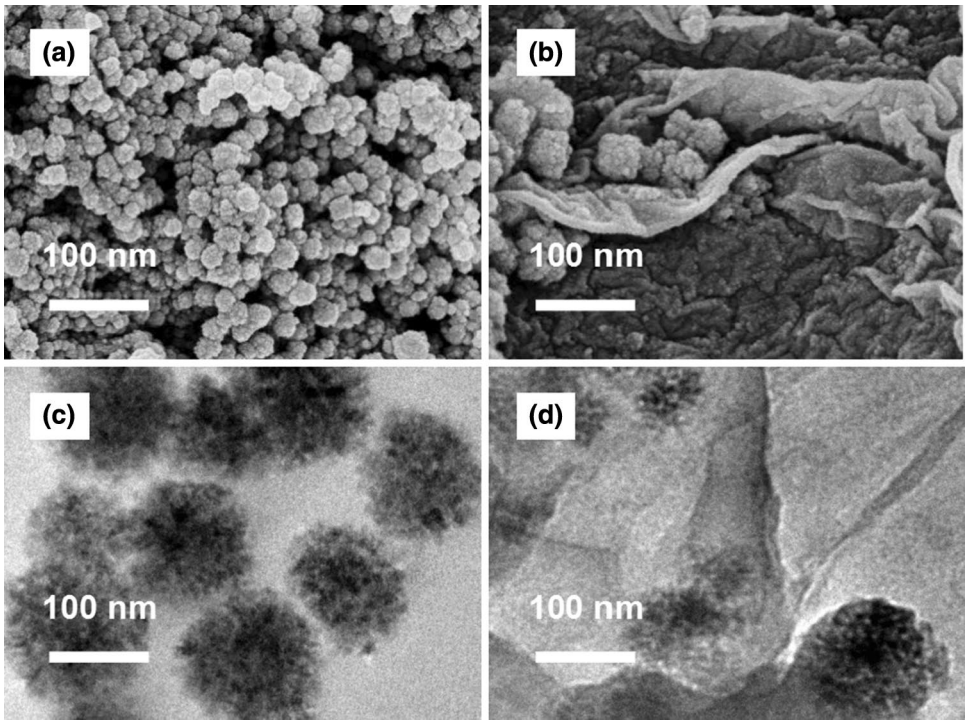

Fig. 2 SEM images of UiO-66/Fe_3O_4 (**a**), UiO-66/Fe_3O_4/GO (**b**), and TEM images of UiO-66/Fe_3O_4 (**c**), UiO-66/Fe_3O_4/GO (**d**)

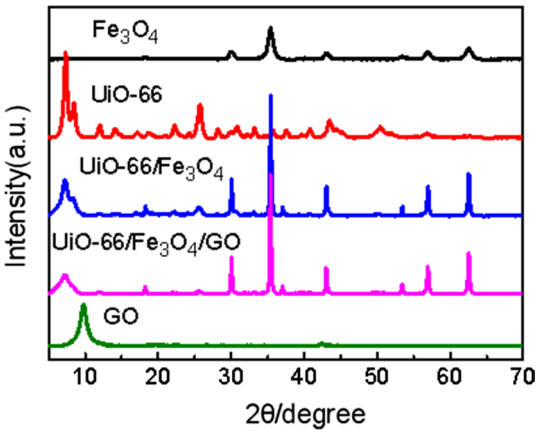

Fig. 3 XRD patterns of Fe_3O_4, UiO-66, UiO-66/Fe_3O_4, UiO-66/Fe_3O_4/GO and GO

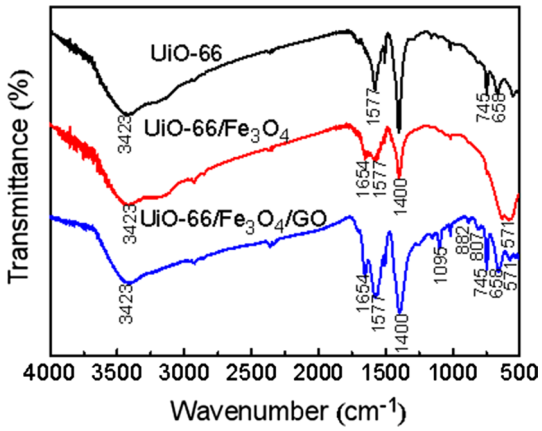

Fig. 4 FTIR images of UiO-66, UiO-66/Fe_3O_4 and UiO-66/Fe_3O_4/GO

UiO-66/Fe_3O_4 and UiO-66/Fe_3O_4/GO pores were highly uniform in pore size and the pore connectivity was well. Moreover the specific surface area of UiO-66/Fe_3O_4/GO was 171.79 $m^2\ g^{-1}$, which was larger than that of UiO-66/Fe_3O_4 (162.37 $m^2\ g^{-1}$), which were shown in Table 1. This was due to the addition of GO, which facilitated the attachment of the nanoparticles to the GO layer, reduced the agglomeration of the UiO-66/Fe_3O_4 nanoparticles, and the incorporation of GO had a positive effect on the specific surface area of the material consistent with previously reported results [24].

The VSM measurements were performed on UiO-66/Fe_3O_4 and UiO-66/Fe_3O_4/GO using a magnetic measurement system. The saturation magnetization (M_s) values of the two materials were 48.06 emu g^{-1} and 15.53 emu g^{-1}, respectively, which can be obtained from the magnetization curve shown in Fig. 6a. According to previous reports, the M_s value of Fe_3O_4 nanoparticles is 69.69 emu g^{-1} [15] and higher than that of UiO-66/Fe_3O_4 and UiO-66/Fe_3O_4/GO, which may be due to the encapsulation of Fe_3O_4 by UiO-66 non-magnetic material and the coverage of UiO-66/Fe_3O_4 nanoparticles by GO. Although the M_s value of the composites were lower compared to that of Fe_3O_4, it was sufficient to separate solid materials from solution by magnets. Besides, when the magnetic

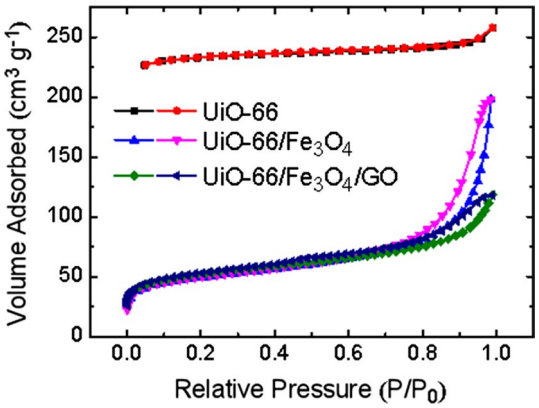

Fig. 5 N_2 adsorption–desorption isotherms of UiO-66, UiO-66/Fe_3O_4 and UiO-66/Fe_3O_4/GO

Table 1 The porous structure parameters of adsorbents

Sample	S_{BET} ($m^2\ g^{-1}$)	Pore volume ($cm^3\ g^{-1}$)	Pore size (nm)
UiO-66	681.38	0.0546	5.4725
UiO-66/Fe_3O_4	162.37	0.2485	15.2933
UiO-66/Fe_3O_4/GO	171.79	0.11162	8.9332

field was applied, the particles dissolved in water were rapidly attracted by the magnet and accumulated on the bottle wall within 15 s, as shown in Fig. 6b. The solution became clear and transparent to achieve the purpose of separation. After removing the magnetic field, the solid adsorbents would be redispersed in water to form a mixed solution.

Adsorption experiments

At a temperature of 298 K and a pH of 7, add 0.01 g of adsorbents to 50 mL of Cs^+ solution with different initial concentration, and shake it at 200 rpm for 12 h with a constant temperature oscillator to investigate the influence of different initial Cs^+ concentration on the adsorption and shown in Fig. 7a. The adsorption amount q_e increased with the ascension of initial Cs^+ concentration and obtained the maximum capacity of 58 ± 2 mg g^{-1}, 60 ± 5 mg g^{-1} and 63 ± 2 mg g^{-1} at an initial Cs^+ concentration of 80 mg L^{-1}, respectively. UiO-66/Fe_3O_4/GO was higher than the other two adsorbents on adsorption capacity, owing to the fact that the addition of GO increased the surface area of the material and the active sites reacted with Cs^+ [24, 29]. At low concentrations, Cs^+ was relatively less competitive than other positive ions. With Cs^+ concentration ascension, Cs^+ occupied the adsorption sites until saturation. When equilibrium was reached, adsorption was accompanied by desorption, which was a reversible reaction [30], the adsorption and desorption were in dynamic equilibrium resulting in the adsorption capacity will no longer increase and may even decrease with increasing concentration.

The change in adsorption capacity of the adsorbents at different contact time was studied under the conditions of temperature 298 K, pH 7, and initial Cs^+ concentration of 60 mg L^{-1}. The experimental results were shown in Fig. 7b, the adsorbent rapidly adsorbed Cs^+ in the first 10 min, on account of sufficient active sites to react with Cs^+ in the initial stage of the reaction [31]. After rapid adsorption phase, the adsorption process slowly increased as the available adsorption sites and nanocavities gradually decrease, reaching equilibrium until 2 h. At this time, the adsorption and desorption amount of Cs^+ were in a dynamic equilibrium state [32]. The experimental results showed that the adsorption rate of the adsorbents synthesized was fast and the equilibrium time was 2 h.

In order to investigate the effect of temperature on adsorption performance, experiments were carried out at pH 7, $t = 12$ h, initial Cs^+ concentration of 60 mg L^{-1} and different temperatures of 298 K, 308 K, 318 K and 328 K,

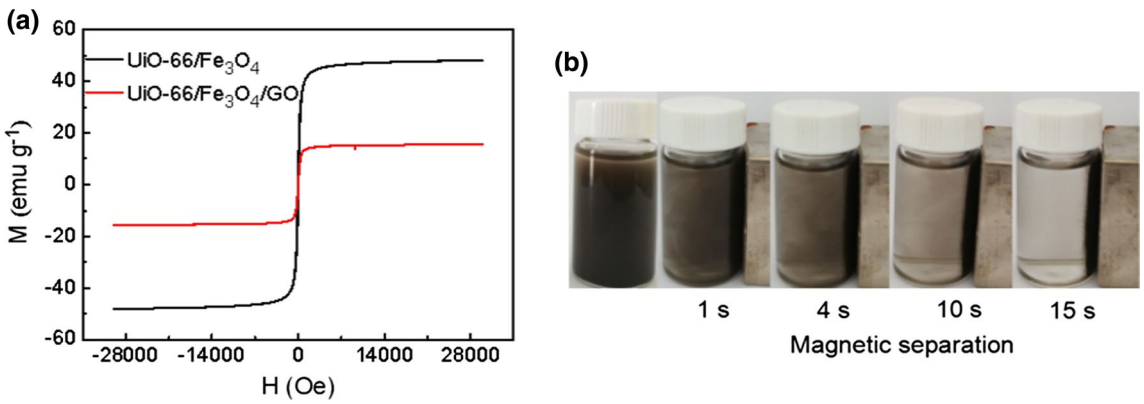

Fig. 6 Magnetic hysteresis loops of UiO-66/Fe_3O_4 and UiO-66/Fe_3O_4/GO (**a**); magnetic separation of UiO-66/Fe_3O_4/GO (**b**)

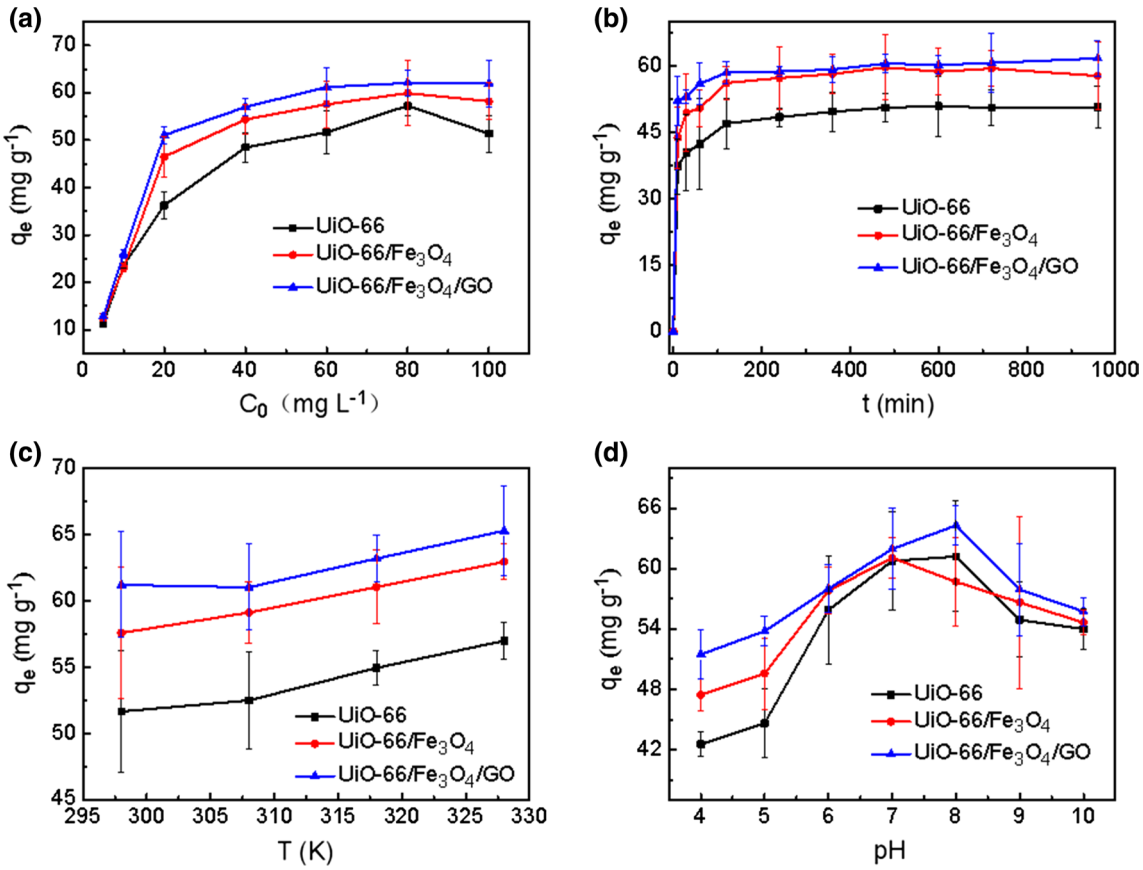

Fig. 7 Effect of initial Cs^+ concentration (**a**), contact time (**b**), temperature (**c**) and pH (**d**) on Cs^+ adsorption

as shown in Fig. 7c. Overall, as the temperature increased from 298 to 328 K, the Cs^+ adsorption trends of UiO-66, UiO-66/Fe_3O_4 and UiO-66/Fe_3O_4/GO were consistent at different temperatures and the capacity acquired maximum 56.99 mg g^{-1}, 62.95 mg g^{-1} and 65.28 mg g^{-1} at 328 K, respectively. The results indicated the endothermic reaction properties of the adsorption process and the thermal stability of these materials.

The different pH of the solution will change the surface charge and stability of the adsorbent, and the presence of Cs^+. Therefore, this experiment studied the adsorption in the wide pH range of 4–10 (Fig. 7d) and maintained $T = 298$ K, $t = 12$ h, initial Cs^+ concentration of 60 mg L^{-1}. These curves showed the tendency rising up at the beginning and declining in late. The adsorption amount q_e reached a maximum at pH 7 or 8. The reasons for the trend of change may be that the material partially dissolved and the Cs^+ also competed with a large amount of H^+ under strong acid conditions [26]. As the pH increased, the H^+ of the solution was neutralized by OH^-, thereby reducing competition with Cs^+, resulting in a rapid increase in the adsorption capacity. Under neutral and alkaline conditions, the materials deprotonation occurred, which increased the amount of negative charges on the surface to enhance the electrostatic adsorption of Cs^+ [33]. Furthermore, the concentration of Na^+ increased rapidly, leading to competition with Cs^+ again, which was not conducive to adsorption [34].

Adsorption mechanism

Adsorption isotherms

The adsorption isotherms are the basic method to study the interaction mode of adsorbent and adsorption, the degree of action and the surface property of the adsorbent. And the adsorption isotherms can be used to describe the adsorption equilibrium, properties and evaluate the maximum adsorption capacity of UiO-66, UiO-66/Fe_3O_4 and UiO-66/Fe_3O_4/GO under equilibrium conditions. Therefore, the experimental results obtained by adding 0.01 g of adsorbent to 50 mL of different initial concentrations of Cs^+ solution under the experimental conditions of $T = 298$ K, pH 7 and $t = 12$ h was used to plot the Langmuir and Freundlich isotherm models [35, 36] to fit the adsorption results. The linear form of the Langmuir model is Eq. (2):

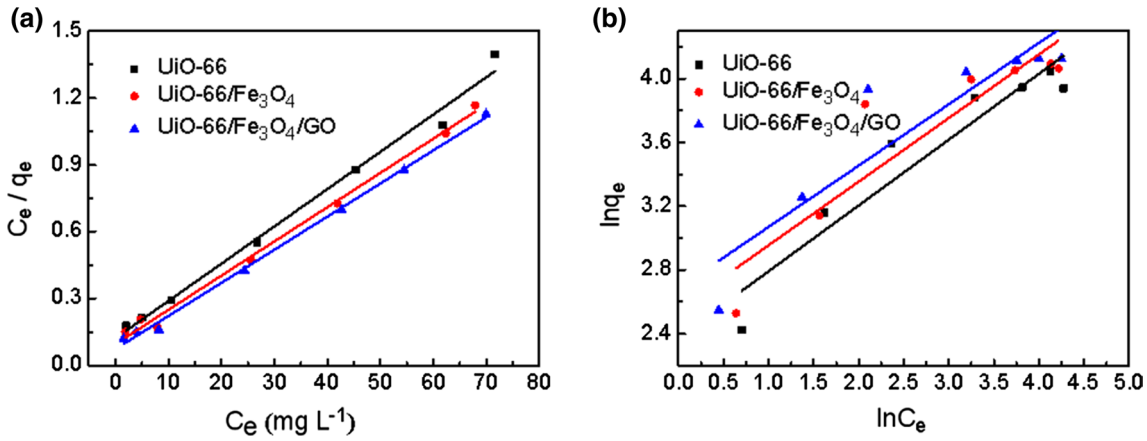

Fig. 8 Langmuir adsorption isotherm (**a**) and Freundlich adsorption isotherm (**b**) of Cs^+ on UiO-66, UiO-66/Fe_3O_4 and UiO-66/Fe_3O_4/GO

$$\frac{C_e}{q_e} = \frac{1}{Q_{max}K_L} + \frac{C_e}{Q_{max}} \tag{2}$$

where q_e (mg g^{-1}) is the adsorption amount of Cs^+ adsorbed by per unit weight of adsorbents, C_e (mg L^{-1}) is the Cs^+ concentration when the adsorption process reaches equilibrium, Q_{max} (mg g^{-1}) is theoretical maximum single-layer adsorption capacity that the adsorbents can achieve, and K_L (L mg^{-1}) is the Langmuir constant. Q_{max} and K_L are calculated from the intercept and slope of these curves fitted the linear relationship between C_e/q_e and q_e in Fig. 8a. Table 2 gives the Langmuir adsorption isotherm parameters values. The maximum q_e of UiO-66, UiO-66/Fe_3O_4 and UiO-66/Fe_3O_4/GO were 57.29 mg g^{-1}, 59.93 mg g^{-1} and 62.07 mg g^{-1}, which were similar to the theoretically maximum capacity Q_{max} value of 59.84 mg g^{-1}, 65.19 mg g^{-1} and 67.39 mg g^{-1} determined by Langmuir isotherm. The experimental maximum adsorption capacity in this study was compared with those obtained in previous studies of Cs^+ adsorption and listed in Table 3. It can be seen that the maximum adsorption amount of UiO-66/Fe_3O_4/GO was higher than that of some known adsorbents, such as natural attapulgite [37], SiO_2–AMP–Cal–Alg [38] and PB/Fe_3O_4/GO [24]. Secondly, the magnetic properties of materials make the absorbent of this study easier to separate from the solution compared with other absorbents, such as Conjugate uprobent [8], PB@pomelo peel [32], Amino-functionalized multi-derivative carbon nanotubes [31]. Furthermore, the addition of GO improves the hydrophilicity and dispersibility of the composites. UiO-66/Fe_3O_4/GO was suitable for the removal of Cs^+. The magnitude of the R^2 indicated the correlation between the Langmuir isotherm and the adsorption properties. The R^2 value of UiO-66, UiO-66/Fe_3O_4 and UiO-66/Fe_3O_4/GO were 0.9890, 0.9936 and 0.9967 respectively, indicating that the adsorption results fitted well with the Langmuir isotherm. It also proved that the adsorption position of the material was single-layered and uniform.

Table 2 Langmuir isotherm constants and their correlation coefficients

Adsorbents	Q_{max} (mg g^{-1})	K_L (L mg^{-1})	R^2
UiO-66	59.84	0.1362	0.9890
UiO-66/Fe_3O_4	65.19	0.1590	0.9936
UiO-66/Fe_3O_4/GO	67.39	0.1999	0.9967

Table 3 Comparison of maximum Cs adsorption capacity q_e for different adsorbents

Adsorbents	q_e (mg g^{-1})	References
Conjugate adsorbent	77.70	[8]
PB/Fe_3O_4/GO	55.56	[24]
Hexacyanoferrate@polyacrylonitrile@magnetite	260	[26]
Amino-functionalized multi-walled carbon nanotubes	136.3	[31]
PB@Pomelo peel	83.8	[32]
MOF/Fe_3O_4/KNiFC	109.0	[33]
Natural attapulgite	2.16×10^{-3}	[37]
SiO_2-AMP-Cal-Alg	37.52	[38]
UiO-66	57.29	This study
UiO-66/Fe_3O_4	59.93	This study
UiO-66/Fe_3O_4/GO	62.07	This study

The dimensionless constant separation factor R_L evaluates the favorability of adsorption reaction in the Langmuir isotherm model, which is calculated by the formula Eq. (3):

$$R_L = \frac{1}{1 + K_L C_L} \tag{3}$$

where C_L (mg L^{-1}) is the highest initial concentration of Cs^+. If the value of R_L is greater than 1, it means that the adsorption reaction in the Langmuir isotherm model is unfavorable; if R_L is equal to 1, it represents that the reaction is linear; if R_L is less than 1 and greater than 0, the reaction is favorable; If R_L is equal to 0, then the reaction is irreversible. The R_L values of UiO-66, UiO-66/Fe_3O_4 and UiO-66/Fe_3O_4/GO were 0.068, 0.059 and 0.047, respectively, all between 0 and 1, thus confirming that all three materials were favorable for Cs^+ adsorption.

The Freundlich isotherm is used to describe heterogeneous systems. The linear form of Freundlich equation is expressed as Eq. (4):

$$\ln q_e = \ln K_F + \frac{1}{n}\ln C_e \tag{4}$$

where K_F is Freundlich isotherm constant indicated adsorption capacity of adsorbents and n is also constant represented the degree of dependence of sorption on the equilibrium concentration when the equilibrium concentration equals to 1. The value of the exponent, $1/n$, represents the type of adsorption process to be favorable physical process ($1/n > 1$), linear ($1/n = 1$), and chemical ($1/n < 1$). Furthermore, the value of $1/n$ closer to 0 illustrates the more heterogeneous the surface [39]. The Freundlich isotherm curves were shown in Fig. 8b, and the relevant parameters were figured according to the graph and listed in Table 4. The $1/n$ values of UiO-66, UiO-66/Fe_3O_4 and UiO-66/Fe_3O_4/GO were observed to be between 0 and 1, and it was judged that the adsorption of Cs^+ by the three adsorbents was chemical adsorption. Comparing the R^2 values of the Langmuir and Freundlich isotherms of the three materials, it was found that the Langmuir isotherm R^2 value was higher than Freundlich. Consequently, the adsorption of Cs^+ by the three materials was more consistent with the Langmuir model.

Table 4 Freundlich isotherm constants and their correlation coefficients

Adsorbents	K_F (mg g^{-1})	$1/n$	R^2
UiO-66	10.80	0.4128	0.8892
UiO-66/Fe_3O_4	12.89	0.3989	0.8067
UiO-66/Fe_3O_4/GO	14.67	0.3846	0.8102

Kinetic sorption models

The pseudo-first-order and pseudo-second-order kinetic models were used to evaluate the adsorption mechanism in this study [30, 40, 41] under the conditions of temperature 298 K, pH 7, and initial Cs^+ concentration of 60 mg L^{-1}. The pseudo-first-order rate equation is described by Eq. (5):

$$\ln\left(q_e - q_t\right) = \ln q_e - k_1 t \tag{5}$$

where q_e (mg g^{-1}) is the adsorption amount of Cs^+ adsorbed by per unit weight of adsorbents when the adsorption process reaches equilibrium, q_t (mg g^{-1}) is the amount at time t, and K_1 (min^{-1}) is the pseudo-first-order kinetic model adsorption rate constant. The values of K_1 and theoretically q_e are determined by the slope and the intercept of the graph in Fig. 9a.

The pseudo-second-order rate equation is described by Eq. (6):

$$\frac{t}{q_t} = \frac{1}{K_2 q_e^2} + \frac{t}{q_e} \tag{6}$$

where q_t (mg g^{-1}) is the adsorption amount of Cs^+ adsorbed by per unit weight of adsorbents at time t, q_e (mg g^{-1}) is the amount at equilibrium theoretically, and K_2 (g mg^{-1} min^{-1}) is the pseudo-second-order rate constant. The magnitude of q_e and K_2 were figured by the slope and intercept of the linear plot of t/q_t versus t curve in Fig. 9b. The value of q_e and K_2 were calculated and listed in Table 5. According to Table 5, the R^2 values of pseudo-second-order kinetic were

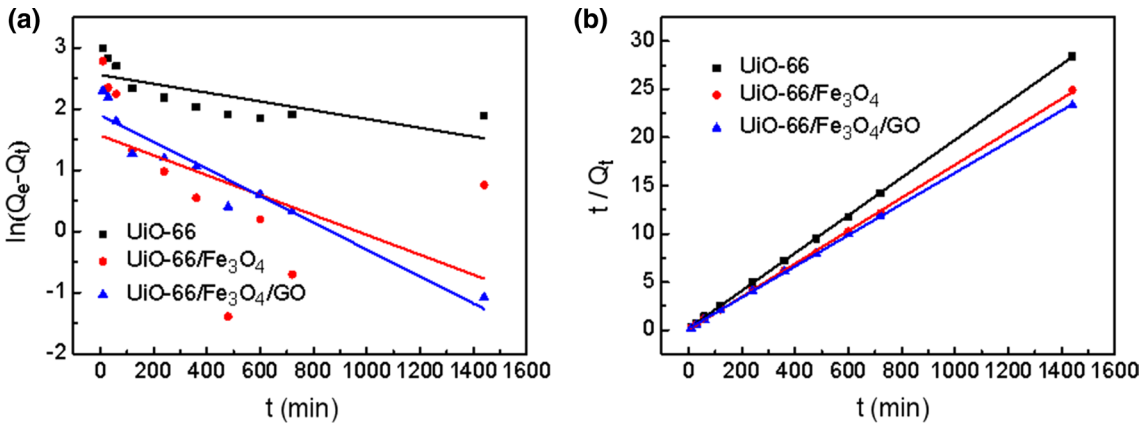

Fig. 9 Pseudo-first-order kinetic (**a**) and Pseudo-second-order kinetic (**b**) of UiO-66, UiO-66/Fe_3O_4 and UiO-66/Fe_3O_4/GO

significantly larger than the pseudo-first-order kinetic for UiO-66, UiO-66/Fe_3O_4 and UiO-66/Fe_3O_4/GO. Furthermore, the experimental measurement of $q_{e,exp}$ was closer to the theoretical $q_{e,cal}$ value of the pseudo-second-order kinetic model. The adsorption of Cs^+ by UiO-66, UiO-66/Fe_3O_4 and UiO-66/Fe_3O_4/GO followed pseudo-second-order kinetic model, which demonstrated that chemisorption limited the kinetic model and rate.

Thermodynamic of sorption

The thermodynamic parameters such as change in enthalpy (ΔH), entropy (ΔS) [40] and Gibbs free energy (ΔG) are determined by using Eqs. (7) and (8):

$$\ln K_D = \frac{\Delta S}{R} - \frac{\Delta H}{RT} \tag{7}$$

$$\Delta G = -RT \ln K_D \tag{8}$$

where K_D ($K_D = q_e/C_e$) is equilibrium distribution constant, and R (8.314 J K^{-1} mol^{-1}) is universal gas constant. The values of ΔS (J K^{-1} mol^{-1}) and ΔH (kJ mol^{-1}) were determined by the curves in Fig. 10. The data in Fig. 10 was obtained under the experiment conditions of pH 7, $t = 12$ h, 60 mg L^{-1} Cs^+ solution and different temperature of 298 K, 308 K, 318 K and 328 K. The ΔG (kJ mol^{-1}) judges the spontaneousness of the adsorption process. The results were shown in Table 6. At $T = 298$, 308, 318 and 328 K, the ΔG of UiO-66, UiO-66/Fe_3O_4 and UiO-66/Fe_3O_4/GO were all lower than 0, demonstrating that the adsorption of Cs^+ on materials was spontaneous and feasible, and the energy required to carry out the reaction. The negative ΔG value increased with temperature addition to reveal that spontaneous adsorption was proportional to temperature. The positive value of ΔH indicated that the interaction between Cs^+ and the adsorbents were endothermic reaction that consumed energy, were consistent with the results reported in the literature [42]. The enthalpy value shows the type of interaction between solid and ion. If the enthalpy is below 40 kJ mol^{-1}, the type of adsorption is a physical process [37]. It can be seen from Table 6 that the ΔH values of all three materials were below 40 kJ mol^{-1}, so the adsorption of Cs^+ were physical adsorption. The positive value of ΔS reflects the affinity of the adsorbent for Cs^+, which was owing to the release of water molecules increased the randomness of the solid/solution interface during adsorption when the Cs^+ was adsorbed on the surface of the adsorbent [1]. Positive ΔH was not conducive to the spontaneous adsorption process, while positive ΔS was advantageous, and $|\Delta H| < |\Delta S|$. Thence, the driving force for enthalpy adsorption on the material was controlled by the entropy effect rather than the enthalpy change [42].

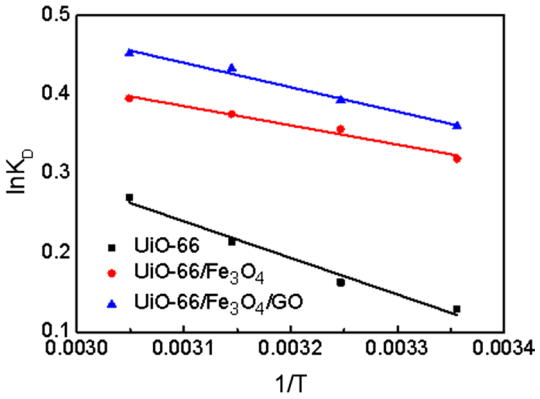

Fig. 10 Thermodynamic of Cs^+ adsorption onto adsorbents

The effect of competing ions

Considering practical applications, most radioactive wastewater contains coexisting non-radioactive ions, such as sodium and potassium, which are chemicals similar to cesium and have similar chemical behavior. Therefore, it is necessary to select sodium ions (Na^+) and potassium ions (K^+) as competitive ions to study the influence of competitive ions on adsorption. In this experiment, 20, 40 and 60 mg L^{-1} of Na^+ or K^+ solution were added to 60 mg L^{-1} of Cs^+ solution. As shown in Fig. 11, in the presence of Na^+ (Fig. 11a) and K^+ (Fig. 11b), the adsorption capacity of UiO-66/Fe_3O_4/GO was more affected than the other two adsorbents, which decreased 55.25 mg g^{-1} and 62.45 mg g^{-1}, respectively. Besides, the effect of K^+ on adsorption was higher than that of Na^+. This phenomenon can be explained by the hydration radius of the ions, which played an important role in the ion exchange and ion trapping of Cs^+ [43].

Table 5 Rate constants and correlation coefficients of the kinetic models

Adsorbents	$q_{e,exp}$ (mg g^{-1})	Pseudo-first-order kinetic			Pseudo-second-order kinetic		
		$K_1 \times 10^{-2}$ (min^{-1})	$q_{e,cal}$ (mg g^{-1})	R^2	$K_2 \times 10^{-2}$ (g mg^{-1} min^{-1})	$q_{e,cal}$ (mg g^{-1})	R^2
UiO-66	57.29	0.07	12.87	0.4805	0.24	51.05	0.9999
UiO-66/Fe_3O_4	59.93	0.16	4.80	0.1967	1.19	58.34	0.9996
UiO-66/Fe_3O_4/GO	62.07	0.22	6.70	0.9126	0.18	61.80	0.9998

Table 6 Thermodynamic parameters of Cs^+ adsorption on adsorbents

Adsorbents	ΔH (kJ mol^{-1})	ΔS (J mol^{-1} K^{-1})	$-\Delta G$ (kJ mol^{-1})			
			298 K	308 K	318 K	328 K
UiO-66	3.84	9.70	0.32	0.42	0.57	0.74
UiO-66/Fe_3O_4	2.02	9.47	0.79	0.91	0.99	1.08
UiO-66/Fe_3O_4/GO	2.56	11.60	0.89	1.01	1.15	1.23

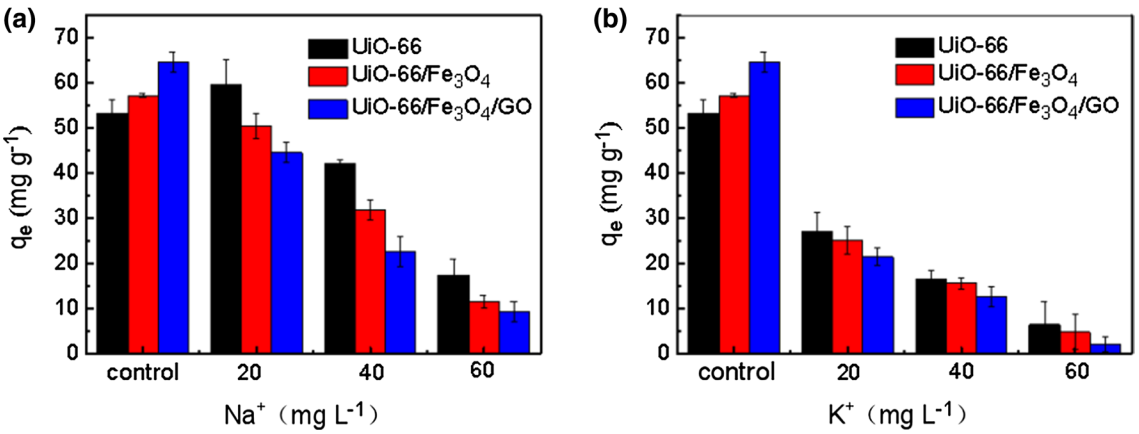

Fig. 11 Cs^+ selectivity in the presence of Na^+ (**a**) and K^+ (**b**)

The hydration radius of Cs^+, K^+ and Na^+ are 3.29 Å, 3.31 Å and 3.58 Å respectively, and that of Cs^+ and K^+ is closer, which is consistent with previous literature reports [44]. In addition, the competitive ions had a significantly higher effect on the adsorption capacity of UiO-66/Fe_3O_4/GO than the other two adsorbents. This may be due to the fact that the –OH of Fe_3O_4 and the –COOH of GO react with Na^+ and K^+ to occupy the adsorption sites, inhibiting and hindering the absorption of Cs^+ [30, 45]. However, preventing the adsorption competition of K^+ with Cs^+ did not become an important problem in practical application because of the low concentration of K^+ in natural water.

The effect of recycled adsorbents on Cs^+ adsorption

The regenerative capacity of the adsorbent is an important indicator for practical application. In order to evaluate the regenerative and reusability of UiO-66, UiO-66/Fe_3O_4, UiO-66/Fe_3O_4/GO as adsorbents, desorption regeneration experiments were carried out. 0.1 mol L^{-1} HCl solution was used as desorption agent and 0.1 mol L^{-1} NaOH solution as regeneration agent, and ethanol and deionized water were used as detergent to complete desorption and regeneration of adsorbents. The effect of continuous adsorption–desorption cycle was studied using Cs^+ solution of 300 mg L^{-1}, and the results were shown in Fig. 12. It indicated that the adsorption capacity of the adsorbent to Cs^+ decreased slowly with the increase of the number of cycles. The adsorption capacity of

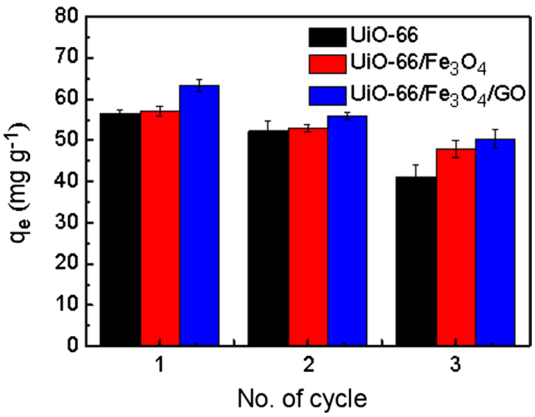

Fig. 12 Reusability of adsorbents for the adsorptive removal of Cs^+

UiO-66/Fe_3O_4/GO for Cs^+ decreased significantly after three cycles, but it was still higher than UiO-66, UiO-66/Fe_3O_4. The composite materials prepared in this study are expected to be applied in practice.

Conclusions

In this study, UiO-66/Fe_3O_4 and UiO-66/Fe_3O_4/GO composites were successfully synthesized to remove Cs^+ from water, and the maximum adsorption amount were 57.29 mg g^{-1} and 62.07 mg g^{-1} respectively. The adsorption behavior of

these adsorbents fitted well with the Langmuir isotherm and the pseudo-second-order kinetic model. They were spontaneous endothermic reaction. Compared with UiO-66/Fe_3O_4 nanoparticles, the UiO-66/Fe_3O_4/GO exhibited remarkably enhanced material stability and Cs^+ removal efficiency. The adsorption capacity can be achieved equilibrium in 2 h, increased 4.07 mg g^{-1} when the temperature increased from 298 to 328 K, and reached maximum at pH 8. The addition of Na^+ and K^+ led to the decrease on the adsorption of Cs^+, and the effect of K^+ was greater than that of Na^+. In addition, Fe_3O_4 made it can be quickly and easily recovered from water by means of magnetic separation to avoid secondary pollution and the preparation process is simple and economical. The prepared UiO-66/Fe_3O_4/GO composite is a promising method for removing Cs^+ from nuclear wastewater.

Acknowledgements The authors sincerely acknowledged financial supports from the National Natural Science Foundation of China (Nos. 41371446, 41271498); the National Social Science Foundation of China (No. 16BJL074) and SKLECRA2014OFP10; Science and Technology Project of Changzhou University (ZMF17020117); Natural Science Fund for Colleges and Universities in Jiangsu Province (18KJB610001); Natural Science Foundation of Jiangsu Province (BK20180964).

References

1. Kadam AA, Jang J, Lee DS (2016) Facile synthesis of pectin-stabilized magnetic graphene oxide Prussian blue nanocomposites for selective cesium removal from aqueous solution. Bioresour Technol 216:391–398. https://doi.org/10.1016/j.biortech.2016.05.103
2. Wang H, Otsu H, Sakurai H, Ahn DS, Aikawa M, Doornenbal P, Fukuda N, Isobe T, Kawakami S, Koyama S (2016) Spallation reaction study for fission products in nuclear waste: cross section measurements for ^{137}Cs and ^{90}Sr on proton and deuteron. Phys Lett B 754(C):104–108
3. Sangvanich T, Sukwarotwat V, Wiacek RJ, Grudzien RM, Fryxell GE, Addleman RS, Timchalk C, Yantasee W (2010) Selective capture of cesium and thallium from natural waters and simulated wastes with copper ferrocyanide functionalized mesoporous silica. J Hazard Mater 182(1):225–231
4. Evangeliou N, Balkanski Y, Cozic A, Møller AP (2014) Global and local cancer risks after the Fukushima Nuclear Power Plant accident as seen from Chernobyl: a modeling study for radiocaesium (^{134}Cs & ^{137}Cs). Environ Int 64(64C):17–27
5. Lee WE (2015) Radioactive waste management and contaminated site clean-up. Elsevier, Woodhead Publishing
6. Mahmoud MR, Seliman AF (2014) Evaluation of silica/ferrocyanide composite as a dual-function material for simultaneous removal of $^{137}Cs^+$ and $^{99}TcO^{4-}$ from aqueous solutions. Appl Radiat Isot 91:141–154. https://doi.org/10.1016/j.apradiso.2014.05.021
7. Khandaker S, Kuba T, Kamida S, Uchikawa Y (2017) Adsorption of cesium from aqueous solution by raw and concentrated nitric acid-modified bamboo charcoal. J Environ Chem Eng 5(2):1456–1464. https://doi.org/10.1016/j.jece.2017.02.014
8. Awual MR, Yaita T, Taguchi T, Shiwaku H, Suzuki S, Okamoto Y (2014) Selective cesium removal from radioactive liquid waste by crown ether immobilized new class conjugate adsorbent. J Hazard Mater 278:227–235. https://doi.org/10.1016/j.jhazmat.2014.06.011
9. Vlasova EA, Yakimov SA, Naidenko EV, Kudrik EV, Makarov SV (2016) Application of metal–organic frameworks for purification of vegetable oils. Food Chem 190:103–109. https://doi.org/10.1016/j.foodchem.2015.05.078
10. Zhang W, Yan Z, Gao J, Tong P, Liu W, Zhang L (2015) Metal–organic framework UiO-66 modified magnetite@silica core–shell magnetic microspheres for magnetic solid-phase extraction of domoic acid from shellfish samples. J Chromatogr A 1400:10–18. https://doi.org/10.1016/j.chroma.2015.04.061
11. Sumida K, Rogow DL, Mason JA, McDonald TM, Bloch ED, Herm ZR, Bae TH, Long JR (2012) Carbon dioxide capture in metal–organic frameworks. Chem Rev 112(2):724–781. https://doi.org/10.1021/cr2003272
12. Kreno LE, Leong K, Farha OK, Allendorf M, Van Duyne RP, Hupp JT (2012) Metal–organic framework materials as chemical sensors. Chem Rev 112(2):1105–1125. https://doi.org/10.1021/cr200324t
13. Lee J, Farha OK, Roberts J, Scheidt KA, Nguyen ST, Hupp JT (2009) Metal–organic framework materials as catalysts. Chem Soc Rev 38(5):1450–1459. https://doi.org/10.1039/b807080f
14. Li JR, Kuppler RJ, Zhou HC (2009) Selective gas adsorption and separation in metal–organic frameworks. Chem Soc Rev 38(5):1477–1504. https://doi.org/10.1039/b802426j
15. Zhao H-X, Zou Q, Sun S-K, Yu C, Zhang X, Li R-J, Fu Y-Y (2016) Theranostic metal–organic framework core–shell composites for magnetic resonance imaging and drug delivery. Chem Sci 7(8):5294–5301. https://doi.org/10.1039/c6sc01359g
16. Ribeiro AM, Campo MC, Narin G, Santos JC, Ferreira A, Chang J-S, Hwang YK, Seo Y-K, Lee UH, Loureiro JM, Rodrigues AE (2013) Pressure swing adsorption process for the separation of nitrogen and propylene with a MOF adsorbent MIL-100(Fe). Sep Purif Technol 110:101–111. https://doi.org/10.1016/j.seppur.2013.03.009
17. Xiao C, Silver MA, Wang S (2017) Metal–organic frameworks for radionuclide sequestration from aqueous solution: a brief overview and outlook. Dalton Trans 46(47):16381–16386. https://doi.org/10.1039/c7dt03670a
18. Shang HB, Yang CX, Yan XP (2014) Metal–organic framework UiO-66 coated stainless steel fiber for solid-phase microextraction of phenols in water samples. J Chromatogr A 1357:165–171. https://doi.org/10.1016/j.chroma.2014.05.027
19. Katz MJ, Brown ZJ, Colon YJ, Siu PW, Scheidt KA, Snurr RQ, Hupp JT, Farha OK (2013) A facile synthesis of UiO-66, UiO-67 and their derivatives. Chem Commun 49(82):9449–9451. https://doi.org/10.1039/c3cc46105j
20. Beheshti H, Irani M, Hosseini L, Rahimi A, Aliabadi M (2016) Removal of Cr(VI) from aqueous solutions using chitosan/MWCNT/Fe_3O_4 composite nanofibers-batch and column studies. Chem Eng J 284:557–564. https://doi.org/10.1016/j.cej.2015.08.158
21. Lv F, Fu L, Giannelis EP, Qi G (2014) Preparation of γ-Fe_2O_3/SiO_2-capsule composites capable of using as drug delivery and magnetic targeting system from hydrophobic iron acetylacetonate and hydrophilic SiO_2-capsule. Solid State Sci 34:49–55. https://doi.org/10.1016/j.solidstatesciences.2014.05.006
22. Lu AH, Salabas EL, Schuth F (2007) Magnetic nanoparticles: synthesis, protection, functionalization, and application. Angew Chem Int Ed 46(8):1222–1244. https://doi.org/10.1002/anie.200602866
23. Li L, Liu XL, Geng HY, Hu B, Song GW, Xu ZS (2013) A MOF/graphite oxide hybrid (MOF: HKUST-1) material for the adsorption of methylene blue from aqueous solution. J Mater Chem A 1(35):10292. https://doi.org/10.1039/c3ta11478c

24. Yang H, Sun L, Zhai J, Li H, Zhao Y, Yu H (2014) In situ controllable synthesis of magnetic Prussian blue/graphene oxide nanocomposites for removal of radioactive cesium in water. J Mater Chem A 2(2):326–332. https://doi.org/10.1039/c3ta13548a
25. Li L, Liu Y, Sun K, He Y, Liu L (2017) One step synthesis of magnetic composite Fe_3O_4/Cu-BTC/GO. Mater Lett 197:196–200. https://doi.org/10.1016/j.matlet.2017.03.004
26. Mobtaker HG, Yousefi T, Pakzad SM (2016) Cesium removal from nuclear waste using a magnetical CuHCNPAN nano composite. J Nucl Mater 482:306–312. https://doi.org/10.1016/j.jnucmat.2016.10.034
27. Zhu C, Guo S, Wang P, Xing L, Fang Y, Zhai Y, Dong S (2010) One-pot, water-phase approach to high-quality graphene/TiO_2 composite nanosheets. Chem Commun 46(38):7148–7150. https://doi.org/10.1039/c0cc01459a
28. Chen Q, He Q, Lv M, Xu Y, Yang H, Liu X, Wei F (2015) Selective adsorption of cationic dyes by UiO-66–NH_2. Appl Surf Sci 327:77–85. https://doi.org/10.1016/j.apsusc.2014.11.103
29. Li L, Liu XL, Gao M, Hong W, Liu GZ, Fan L, Hu B, Xia QH, Liu L, Song GW, Xu ZS (2014) The adsorption on magnetic hybrid Fe_3O_4/HKUST-1/GO of methylene blue from water solution. J Mater Chem A 2(6):1795–1801. https://doi.org/10.1039/c3ta14225f
30. Zheng X, Dou J, Yuan J, Qin W, Hong X, Ding A (2017) Removal of Cs^+ from water and soil by ammonium-pillared montmorillonite/Fe_3O_4 composite. J Environ Sci (China) 56:12–24. https://doi.org/10.1016/j.jes.2016.08.019
31. Jang J, Miran W, Lee DS (2018) Amino-functionalized multi-walled carbon nanotubes for removal of cesium from aqueous solution. J Radioanal Nucl Chem 316(2):691–701. https://doi.org/10.1007/s10967-018-5812-6
32. Chang S, Chang L, Han W, Li Z, Dai Y, Zhang H (2018) In situ green production of Prussian blue/natural porous framework nanocomposites for radioactive Cs^+ removal. J Radioanal Nucl Chem 316(1):209–219. https://doi.org/10.1007/s10967-018-5767-7
33. Naeimi S, Faghihian H (2017) Performance of novel adsorbent prepared by magnetic metal–organic framework (MOF) modified by potassium nickel hexacyanoferrate for removal of Cs^+ from aqueous solution. Sep Purif Technol 175:255–265. https://doi.org/10.1016/j.seppur.2016.11.028
34. Yang P, Liu Q, Liu J, Zhang H, Li Z, Li R, Liu L, Wang J (2017) Interfacial growth of metal organic framework (UiO-66) on the functionalization of graphene oxide (GO) as a suitable seawater adsorbent for extraction of uranium(VI). J Mater Chem A 5(34):17933–17942. https://doi.org/10.1039/c6ta10022h
35. Ali RM, Hamad HA, Hussein MM, Malash GF (2016) Potential of using green adsorbent of heavy metal removal from aqueous solutions: adsorption kinetics, isotherm, thermodynamic, mechanism and economic analysis. Ecol Eng 91:317–332. https://doi.org/10.1016/j.ecoleng.2016.03.015
36. Rearte TA, Bozzano PB, Andrade ML, Fabrizio de Iorio A (2013) Biosorption of Cr(III) and Pb(II) by *Schoenoplectus californicus* and insights into the binding mechanism. ISRN Chem Eng 2013:1–13. https://doi.org/10.1155/2013/851602
37. Kilincarslan Kaygun A, Eral M, Akyil Erenturk S (2016) Removal of cesium and strontium using natural attapulgite: evaluation of adsorption isotherm and thermodynamic data. J Radioanal Nucl Chem 311(2):1459–1464. https://doi.org/10.1007/s10967-016-4989-9
38. Saha S, Singhal RK, Basu H, Pimple MV (2016) Ammonium molybdate phosphate functionalized silicon dioxide impregnated in calcium alginate for highly efficient removal of ^{137}Cs from aquatic bodies. RSC Adv 6(98):95620–95627. https://doi.org/10.1039/c6ra20283g
39. Liu H, Xie S, Wang T, Liu Y, Zeng T (2017) Effect of coexisting cations on the adsorption of cesium onto poly (β-cyclodextrin)/bentonite composite. J Radioanal Nucl Chem 312(3):557–565. https://doi.org/10.1007/s10967-017-5256-4
40. Tan IA, Ahmad AL, Hameed BH (2009) Adsorption isotherms, kinetics, thermodynamics and desorption studies of 2,4,6-trichlorophenol on oil palm empty fruit bunch-based activated carbon. J Hazard Mater 164(2–3):473–482. https://doi.org/10.1016/j.jhazmat.2008.08.025
41. Qiu H, Lv L, Pan B-c, Zhang Q-j, Zhang W-m, Zhang Q-x (2009) Critical review in adsorption kinetic models. J Zhejiang Univ Sci A 10(5):716–724. https://doi.org/10.1631/jzus.A0820524
42. Lyu J, Liu H, Zeng Z, Zhang J, Xiao Z, Bai P, Guo X (2017) Metal–organic framework UiO-66 as an efficient adsorbent for boron removal from aqueous solution. Ind Eng Chem Res 56(9):2565–2572. https://doi.org/10.1021/acs.iecr.6b04066
43. Yang S, Okada N, Nagatsu M (2016) The highly effective removal of Cs^+ by low turbidity chitosan-grafted magnetic bentonite. J Hazard Mater 301:8–16. https://doi.org/10.1016/j.jhazmat.2015.08.033
44. Alamudy HA, Cho K (2018) Selective adsorption of cesium from an aqueous solution by a montmorillonite-prussian blue hybrid. Chem Eng J 349:595–602. https://doi.org/10.1016/j.cej.2018.05.137
45. Nam SW, Jung C, Li H, Yu M, Flora JR, Boateng LK, Her N, Zoh KD, Yoon Y (2015) Adsorption characteristics of diclofenac and sulfamethoxazole to graphene oxide in aqueous solution. Chemosphere 136:20–26. https://doi.org/10.1016/j.chemosphere.2015.03.061